

# High efficiency quantum memory for linear optics quantum information applications

James Stuart, Kieran Smith, Morgan Hedges, Rose Ahlefeldt, and Matthew Sellars

Optical quantum memories based on Er, with its telecom-compatible optical transition, could benefit quantum networking and linear optics quantum computing applications, if the application requirements for high memory efficiency, fidelity, and storage capacity can be met. Here, we demonstrate the first high efficiency quantum memory in Er, with spin-state storage for 25  $\mu$ s and efficiencies up to 81%, using the rephased amplified spontaneous emission protocol. We show high-fidelity entanglement of an output state and the state stored in memory, and initial demonstrations of the multiplexing capacity, storing 70 modes in the temporal domain. We use the results to discuss how, with modifications to the pulse sequences and experimental geometry only, the performance can be improved to meet the requirements for practical applications.

## I. INTRODUCTION

Significant advances in the algorithms and hardware for linear optics quantum computing (LOQC) have driven major commercial efforts to build scalable, fault-tolerant linear optics quantum computers (including by PsiQuantum, Xanadu, and OptQC). These enterprises all implement the critical operation of synchronising temporally separated optical modes [1] through a series of fixed fiber-optic delay lines connected to optical switch arrays to create controllable delays. All components of the quantum computer, including these delay lines, must have low loss to allow fault-tolerant algorithms to be implemented [2–4]. Thus, the intrinsic propagation losses of optical fiber (40 dB/ms of storage time in telecom fibers) limit mode delay times to tens of microseconds. These short delay times have flow-on consequences for the rest of the computer, requiring ultra-fast switches, sources, detectors, and electronics to reach the bandwidths needed to create the entangled states for quantum computing [2].

This restriction on the operating regime could be loosened by replacing delay lines and switch arrays with on-demand optical quantum memories implemented in atomic ensembles. An ensemble coherence time of only 1 ms is required to match the 40 dB/ms decay rate of fiber, and atomic ensembles can have coherence times out to seconds or hours [5]. However, the overall efficiency of the memory must also be considered. The best quantum memories demonstrated to date have efficiencies above 70% [6–12], reaching 94.6% (0.24 dB loss) for Rb gas ensembles [12]. This is comparable with the  $\mathcal{O}(0.1)$  dB chip-to-fiber insertion loss achieved in the best available quantum computing chips [13], ignoring the additional losses associated with switching and multiple passes through fiber loops involved in a typically storage stage in current LOQC. Memory performance, then, is approaching the realm where these systems become an attractive competitor to fiber delay lines and switch arrays. Additional benchmarks do need to be met, including memory fidelity above 99%, and compatibility with the telecom wavelengths used in the quantum computer, although these benchmarks are less challenging than high efficiency.

While LOQC applications of quantum memories are

well recognised, most experimental development of quantum memories to date has focused on a different application, quantum repeaters [14–16], where delay lines are not a viable option. For repeaters, long storage time is paramount because the storage time determines the size of the network, with hundreds of milliseconds required for a global network [17]. Otherwise, the requirements for repeaters are similar to LOQC, with efficiencies above 90% [17, 18], near unity fidelity, and telecom compatibility. No fixed thresholds have been set for data capacity, but to allow MHz data rates, for instance, storage of 500 modes is needed in a 100 km network, and 100,000 modes in a global network. Thus, a quantum memory developed to meet the requirements for quantum repeater applications is likely also suitable for LOQC.

One attractive class of candidates for both applications is  $^{167}\text{Er}$ -based crystals.  $^{167}\text{Er}$  has an optical transition in the telecom c-band, where the lowest-loss photonic components are available. Long coherence times can be achieved on its optical (4 ms [19]) and hyperfine (1.3 s [20]) transitions by choosing low decoherence materials such as  $\text{Y}_2\text{SiO}_5$  and applying high magnetic fields.  $^{167}\text{Er}$  also has small optical inhomogeneous linewidths (150 MHz in  $\text{Y}_2\text{SiO}_5$ ) compared to its  $\mathcal{O}(\text{GHz})$  hyperfine splittings (800 MHz in  $\text{Y}_2\text{SiO}_5$ ), which, coupled with its long hyperfine lifetime (180 s [21]) in high fields, allows spectral preparation of the ensemble into a pure state. The complete control over the atomic state offered by this feature allows high bandwidth operation (for high storage capacity) while retaining access to long hyperfine storage times, in contrast to materials where pure state preparation is not possible.

A small number of quantum memory protocols have been demonstrated to date in  $^{167}\text{Er}^{3+}:\text{Y}_2\text{SiO}_5$ : a non-classical two-level atomic frequency comb (AFC) with an efficiency of 22% [21] and two classical two-level revival of silenced echo (ROSE) demonstrations with efficiencies up to 44% [22, 23], all in  $\text{Y}_2\text{SiO}_5$ . These results demonstrate the potential of  $^{167}\text{Er}$ , with efficiencies limited by technical issues rather than fundamental material limitations, but none of the demonstrations have used a memory protocol capable of the simultaneous high efficiency, fidelity, and storage capacity required for repeater and LOQC applications (along with long storage times for repeaters).

Here, we implement the simplest memory protocol with the potential to meet these requirements, rephased amplified spontaneous emission, in  $^{167}\text{Er}^{3+}:\text{Y}_2\text{SiO}_5$ , demonstrating simultaneous storage of tens of modes with efficiencies up to 81% and high fidelity.

## II. EXPERIMENT

### A. Material and spectral preparation

All experiments in this work used the  $^4\text{I}_{15/2}$  to  $^4\text{I}_{13/2}$  optical transition in site 2 of a 0.005%  $^{167}\text{Er}^{3+}:\text{Y}_2\text{SiO}_5$  crystal, grown by Scientific Materials, with an isotopic purity of 92%. The crystal had dimensions of  $3 \times 4 \times 5$  mm cut along the optical extinction axes ( $D_1 \times D_2 \times b$ ) [24]. To suppress the electron spin flips, which lead to excessive decoherence and short hyperfine lifetimes in erbium crystals, the same regime as identified in earlier work [20] was used: the crystal was cooled to 1.5 K in a pumped liquid helium cryostat and a magnetic field of 6 T was applied. This field was aligned  $\sim 1^\circ$  off the crystal's  $D_1$  axis to spectrally separate the magnetically inequivalent subgroups of erbium ions [25]. All experiments were then performed on a single subgroup. Optical access to the crystal was only available through a single window at the bottom of the cryostat. Light entered via this window, propagating  $\sim 1^\circ$  off the  $D_1$  axis, and was reflected back through the crystal by a mirror. All measurements were made in this double pass configuration, with the small angle separating the two beams chosen to avoid optical standing waves across the crystal.

In the above regime, the  $^4\text{I}_{15/2}$  to  $^4\text{I}_{13/2}$  transition chosen has an optical coherence time of 1.35 ms [26] and a hyperfine coherence time of 1.3 seconds [20]. Further, the  $\mathcal{O}(100\text{ s})$  hyperfine lifetime means the population can be readily spectrally prepared into very high optical depth features on minimal absorption backgrounds via optical pumping. The preparation used here involves first optically pumping the entire ensemble into a single hyperfine state ( $|\pm\frac{7}{2}\rangle$ ) [20, 21] possible since the hyperfine structure is optically resolved. Then, an  $\mathcal{O}(\text{MHz})$  sub-ensemble is pumped into the opposite hyperfine state ( $|\mp\frac{7}{2}\rangle$ ) [21], achieving a large spectral and angular momentum separation between this memory feature and the bath of unused erbium ions that limits relaxation pathways for the memory ions.

Using this regime and spectral preparation process, a two-level atomic frequency comb (AFC) [21] was previously demonstrated with an efficiency of 22% almost two orders of magnitude higher than earlier, low-field memory demonstrations in erbium [27, 28]. The 22% efficiency was ultimately limited by background absorption at the memory frequency. Here, we address this issue and apply the same spectral preparation process to the more sophisticated four-level rephased amplified spontaneous emission protocol.

### B. Memory protocol

Four-level rephased amplified spontaneous emission (4-level RASE [29, 30]) is a spin-wave quantum memory protocol that creates two entangled, time-separated optical states [30, 31], where the second optical state is stored and recalled from the ensemble. The 4-level RASE protocol is, thus, a source of entangled light states, allowing it to replace both the quantum light source and the quantum memory components of a quantum network or LOQC architecture.

The 4-level RASE protocol is depicted in Figure 1. The first state is amplified spontaneous emission, ASE, generated from an inverted ensemble. The ASE light state is entangled with the atomic state on the optical levels of the erbium ions. This atomic state is then stored on the hyperfine-levels using a  $\pi$ -pulse ( $\pi_1$ ), and then recalled after a programmable time delay ( $t_b$ ) by a second  $\pi$ -pulse ( $\pi_2$ ). The resulting state emitted from the ensemble is rephased amplified spontaneous emission, RASE, time-symmetric with the original ASE state. The hyperfine storage enables on-demand recall. Very long storage times on the hyperfine state, out to the hyperfine coherence time, are also possible with a modification to the protocol to add hyperfine rephasing pulses. As depicted in Figure 1, an inverted-four-level echo (I4LE) protocol [32] can be implemented at the same time as RASE by probing the ASE transition with a weak, coherent pulse, a method used here to characterise the memory. In this case, the ensemble emits both RASE and an echo of the probe [32]. RASE itself is not a read-write quantum memory because it does not have an input, and due to the gain arising from the inversion, I4LE is not capable of quantum storage. However, the 4-level RASE protocol can be transformed into the noiseless photon echo (NLPE) protocol [33], a read-write memory, with only minor changes to the pulse sequence in Figure 1 (see Sec. IV), so the results here inform on the performance of read-write quantum memories in  $^{167}\text{Er}^{3+}:\text{Y}_2\text{SiO}_5$ .

RASE was first demonstrated in  $\text{Pr}:\text{Y}_2\text{SiO}_5$  using the two-level protocol [29], followed by demonstrations of the 4-level RASE and I4LE protocols in the same material [30–32]. Non-classical correlations were observed [31], with optimised recall efficiencies of 14% [32]. In both demonstrations, the low recall efficiency was attributed to the distortion of the rephasing  $\pi$ -pulses at higher optical depths, so the peak efficiency was reached at a low optical depth of  $\alpha L \approx 1$  [32]. Pulse distortion arises when bright pulses are applied on transitions with high oscillator strengths, unavoidable in  $\text{Pr}:\text{Y}_2\text{SiO}_5$  since the only available transitions for the  $\pi$ -pulses have similar oscillator strengths to the ASE and RASE transitions. In contrast, the four-level system chosen here for  $^{167}\text{Er}:\text{Y}_2\text{SiO}_5$  (Fig. 1) has oscillator strengths on the control pulse transitions of 3.2% ( $\pi_i$ ), 7.3% ( $\pi_1$ ), and 7.0% ( $\pi_2$ ) relative to the ASE transition (see Supplementary Information). The longer optical and spin coherence times of  $^{167}\text{Er}^{3+}:\text{Y}_2\text{SiO}_5$  also benefit the protocol effi-

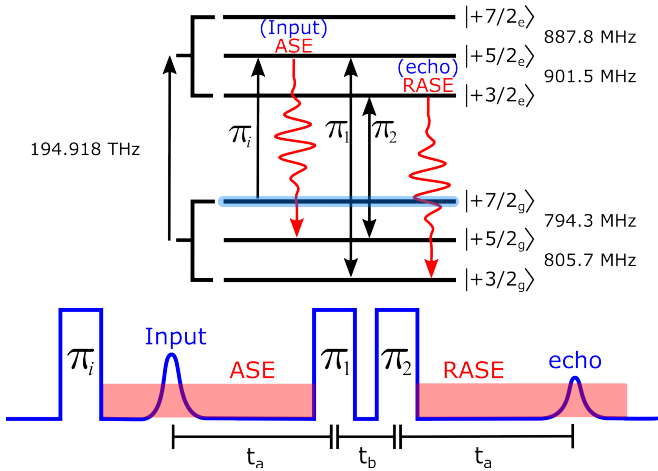


FIG. 1. 4-level RASE protocol. **Top:** level diagram indicating the optical transitions used for RASE. The ensemble was spin polarised into the  $|-\frac{7}{2}_g\rangle$  and a narrow, MHz wide, feature was prepared into the  $|+\frac{7}{2}_g\rangle$  hyperfine level (highlighted in blue). **Bottom:** RASE pulse sequence with an added input pulse to provide an echo (I4LE). The separation between  $\pi_1$  and  $\pi_2$  defines the memory storage time  $t_b$ . The gain on the ASE transition can be controlled by attenuating  $\pi_i$ .

ciency, storage time, and storage capacity.

### C. Experimental setup

The experimental setup, Figure 2, was similar to Ref. [21]. The spectral preparation was also similar: the ensemble was spin polarised into the  $|-\frac{7}{2}_g\rangle$  hyperfine level and then a 1 MHz wide sub-ensemble was prepared into the  $|+\frac{7}{2}_g\rangle$  hyperfine level. All experiments were performed on this sub-ensemble.

Figure 1 shows the experimental pulse sequence. We used the 4-level RASE sequence with an added input pulse on the ASE transition to record an I4LE simultaneously with RASE. The I4LE's input and echo were used as a diagnostic measurement to verify the gain and rephasing efficiency for each shot of data. Several practical considerations influenced the choice of pulse intensities and timing. First, the gain on the ASE transition, which could be controlled by changing the amplitude of  $\pi_i$  at fixed duration, reached a maximum of  $\approx 36$  dB when  $\pi_i$  was a  $\pi$ -pulse. At this high gain, the I4LE input pulses had to be kept weak to avoid over-driving the ensemble; to meet this condition, we used  $\ll 0.1\%$  of a  $\pi$ -pulse. Second, the time delay between the input and rephasing pulses,  $t_a$ , was chosen to be long enough ( $> 10 \mu\text{s}$ ) that an ASE signal could be detected between the I4LE input pulse and the rephasing  $\pi$ -pulses, except for the results in Section III A. A balanced heterodyne detection system was used to detect all output fields. The ASE/input and RASE/echo signals were recorded at the same heterodyne beat frequency, 13 MHz, by phase-

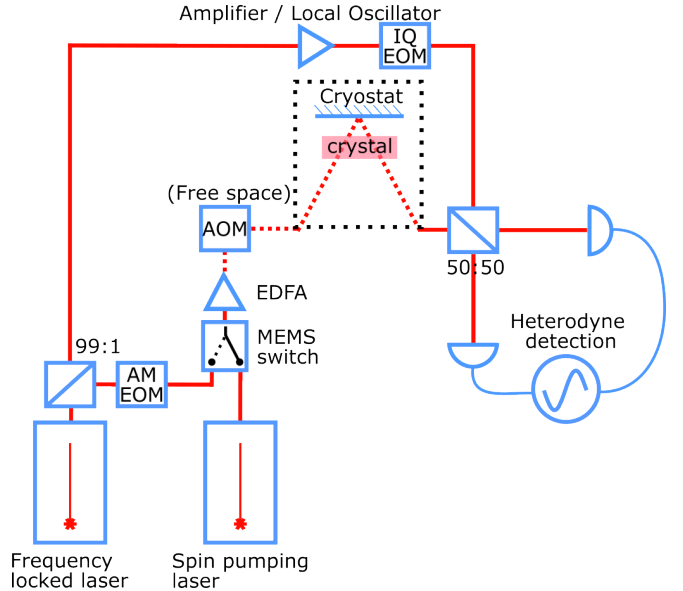


FIG. 2. Experiment setup. Two lasers were used: a frequency locked laser for the RASE sequence, and a spin-pumping laser for spectral preparation into a single hyperfine state [21]. The free space acousto-optic modulator (AOM) was used to gate ASE produced by the erbium-doped fiber amplifier (EDFA) during the RASE experiments. Otherwise, broadband ASE produced by the EDFA drives the ASE transitions and acts as background noise in the RASE window. The local oscillator was an amplified pick-off of the frequency-locked laser passed through an in-phase and quadrature electro-optic modulator (IQ EOM) that was operating in carrier-suppressed single-sideband mode. Operating this way meant only one sideband from the amplitude-modulating EOM (AM EOM) was detected.

coherently switching the frequency of the local oscillator during the rephasing pulses,  $\pi_1$  and  $\pi_2$ . The  $\pi_i$ ,  $\pi_1$ , and  $\pi_2$  pulses were all applied to transitions at least 800 MHz detuned from the local oscillator, well beyond the bandwidth of the detection system. In addition to the RASE sequence pulses, three phase-reference pulses with heterodyne beat frequencies of 8, -12, 15 MHz were added to the sequence to correct for trigger time jitter on the oscilloscope and interferometer phase noise on the heterodyne detection [6, 21]. Figure 3 (A) shows the heterodyne time trace of a high-gain I4LE shot. 60  $\mu\text{s}$  windows, used when analysing each shot, are highlighted for the ASE and RASE fields along with a vacuum window (with only the local oscillator on), used as a noise reference. ASE was emitted at all times between  $\pi_i$  and  $\pi_1$ , as seen by the increase in noise relative to the vacuum window. In this high gain regime, the correlations between the ASE and RASE fields can easily be observed by eye in a single shot, Figure 3 (B). There, the ASE/RASE windows have been digitally beaten to homodyne and overlapped. The RASE signal  $R(t)$  was transformed to match the ASE window using

$$R(t)' = \bar{R}(-t)/\eta \cdot e^{t_a/T} \cdot e^{i\theta}. \quad (1)$$

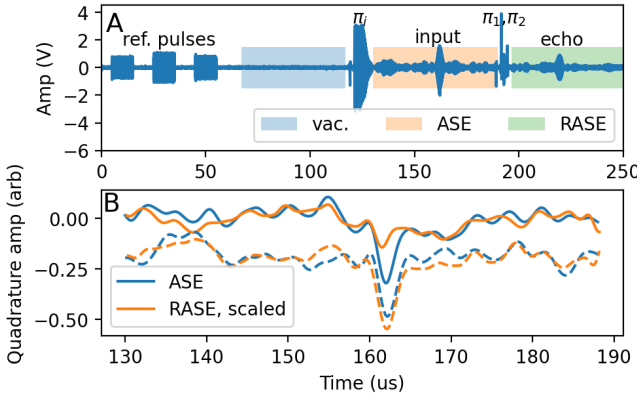


FIG. 3. **A.** High gain I4LE time trace illustrating the experimental pulse sequence, with the windows used for ASE, RASE, and the vacuum reference highlighted. Three phase-correcting reference pulses were used to account for phase and timing jitter between experimental shots. **B.** Comparison of ASE and RASE fields for the high gain data. The fields have been digitally beaten to homodyne and the RASE field has been transformed to match the ASE field (Equ. (1)). The solid lines are the in-phase component of the two fields, while the dashed lines are the out-of-phase components, offset vertically.

This transformation takes the time-reversed complex conjugate of the RASE field, scales it by the rephasing efficiency ( $\eta$ ), accounts for the dephasing that occurred while the field was stored on the optical transition, characterised by the write-time  $T$ , and adds a phase shift ( $\theta$ ) between the ASE and RASE fields. These three parameters were independently measured; the efficiency and phase shift were determined from the I4LE and the decay time was measured from the data in Figures 4 and 5. The solid lines in Figure 3 (B) are the in-phase component of the ASE and RASE field amplitude, while the dashed lines are the out-of-phase components. The I4LE input and echo also appear at 165  $\mu$ s. The strong correlation between the ASE and RASE fields is evident in the clear overlap of the two signals.

### III. RESULTS

Here, we present results from a series of experiments arranged into three categories: I4LE, classical RASE, and non-classical RASE results.

#### A. Inverted-four-level echo

To characterise the recall efficiency and storage time of the protocol and level scheme outlined in Figure 1, we performed a series of I4LE experiments investigating the gain on the ASE transition, the rephasing efficiency, and the effect of the delay times ( $t_a$  and  $t_b$ ).

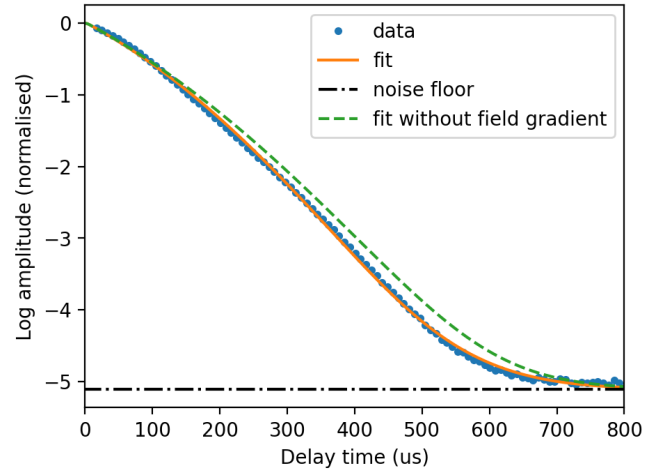


FIG. 4. I4LE write-time. The echo amplitude for an I4LE is shown as a function of delay time ( $2t_a + t_b$ ) between the input pulse and the echo. Here  $t_b$  was fixed at 0.1  $\mu$ s and  $t_a$  varied from 10 to 400  $\mu$ s. The fit accounts for inhomogeneous spin dephasing and a magnetic field gradient across the sample (explained in Supplementary Information). From the fit, we measure a 157.8  $\mu$ s write-time and predict 165  $\mu$ s without the field gradient.

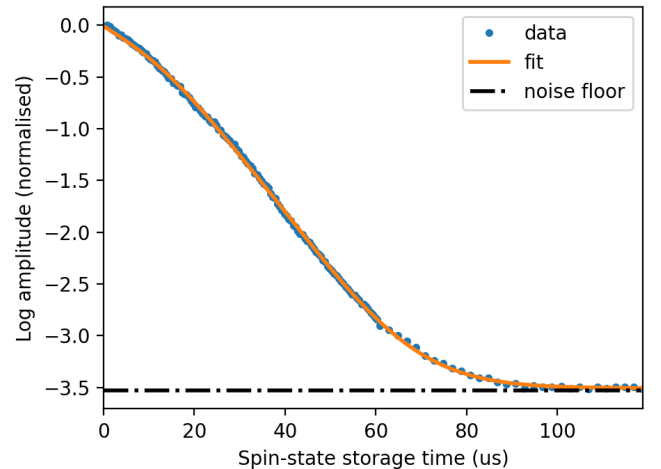


FIG. 5. I4LE spin-state storage. The spin-state storage time of the I4LE was measured by changing  $t_b$ , the time between the two rephasing  $\pi$ -pulses, while  $t_a$  was fixed at 10  $\mu$ s. The fit accounts for inhomogeneous spin dephasing and a magnetic field gradient across the sample (explained in Supplementary Information). The fit gives a 25.1  $\mu$ s spin-state storage time.

Figure 4 shows the echo amplitude as a function of  $t_a$  for a fixed  $t_b = 0.1 \mu$ s, and Figure 5 shows the echo amplitude as a function of  $t_b$  for a fixed  $t_a = 10 \mu$ s. The decay constant in Figures 4 and 5 determine the write-time and spin-state storage time of the memory, respectively.

An upper limit on the write-time is given by the optical coherence time of 1.35 ms [26] and, similarly, the

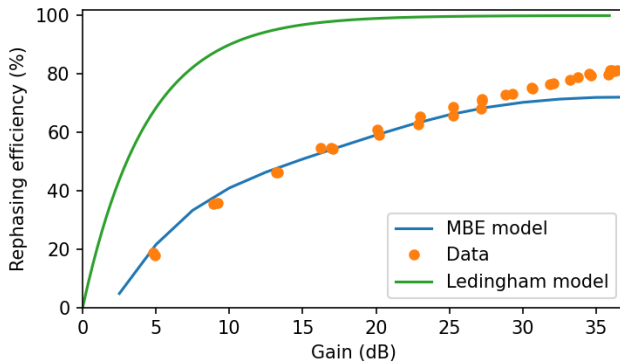


FIG. 6. I4LE efficiency as a function of the gain on the input transition,  $|+\frac{5}{2}\rangle_g \rightarrow |+\frac{5}{2}\rangle_e$ , with delay times  $t_a = 6 \mu\text{s}$  and  $t_b = 0.1 \mu\text{s}$ . The gain was measured by comparing the amplified input pulse to the pulse recorded without a gain medium. The Ledingham model comes from Equation (2). The MBE model was developed to account for background absorption and imperfect rephasing.

storage time's upper limit is given by the hyperfine coherence time of 1.3 s [20]. The decays observed are far faster than these limits, and they are non-exponential. The short decay times and non-exponential behaviour in both sets of data arise from the same effect: “inhomogeneous spin dephasing” [34–36], which arises when the hyperfine transition frequencies in the ground and excited state are not perfectly correlated with each other and the optical transition frequency. The decay profile seen is given by the Fourier transform of the relevant inhomogeneous line shape. For the storage time, the decay is determined by the inhomogeneous spin dephasing on the ground state hyperfine transition. Dephasing due to this frequency distribution can be easily corrected by applying microwave rephasing pulses on this hyperfine transition, but such pulses were not applied here. For the write-time, the decay is determined by the difference in frequencies of individual ions between the ASE and RASE transitions, since the rephasing is only perfect when these are identical. For the transitions chosen here (Fig. 1), this difference is given by the difference in ground and excited state hyperfine frequencies. Because the dephasing arises from the difference of two transitions, rephasing pulses cannot be applied to reverse it, placing a fundamental limit on the write-time.

In addition to inhomogeneous spin dephasing, there is some broadening due to a magnetic field gradient across the 3 mm crystal. With the crystal in the center of the superconducting magnet, the latter effect is small, contributing  $\approx 100$  Hz of broadening (see Supplementary Information, and the intrinsic linewidths can be extracted by fitting the decay profiles in Figures 4 and 5. In both cases, the broadening approximates a Voigt profile. The extracted ground state linewidth of 14.8 kHz is smaller than the linewidths seen for optically-selected subgroups in other rare earth-doped YSO crystals (e.g. Pr, 26 kHz

[35] and Eu, 69 kHz [37]), which we attribute to Er's lower nuclear magnetic sensitivity. The linewidth extracted from the write-time data is lower, 4.3 kHz, indicating a moderate degree of correlation in the excited and ground state hyperfine frequencies. The  $e^{-1}$  point of the two decays give a storage time of 25.1  $\mu\text{s}$  and a write-time of 157.8  $\mu\text{s}$ .

Figure 6 shows the I4LE rephasing efficiency for a series of gains on the input/ASE transition, with  $t_a = 6 \mu\text{s}$  and  $t_b = 0.1 \mu\text{s}$ . The gain was measured by comparing the intensity of the input pulse with, and without,  $\pi$ -pulses applied to the sub-ensemble. The rephasing efficiency increased with gain up to a peak efficiency of 81% at 36 dB. Also shown are two models for the efficiency data. The first (the Ledingham model) is derived in Refs. [32, 38] using theory presented by Ledingham *et al.* [29]. This model treats the ideal case, applying a series of simplifications: a two level system, a homogeneous driving field (spatially and spectrally), no background absorption, no decoherence, and no dispersive effects from the gain feature, to give an efficiency:

$$\eta = \frac{8 \sinh^2(\frac{\alpha L}{2})}{2e^{\alpha L} - 2}, \quad (2)$$

where  $\alpha L$  is the gain on the ASE transition. At all gains, there is a large discrepancy between this idealized model and the data. The second theoretical line comes from a numerical Maxwell-Bloch model that relaxes some of the above assumptions to get a better fit, allowing a non-unity rephasing efficiency and non-zero background absorption. Here “rephasing efficiency” is a catch-all term that includes all losses, other than background absorption, as an instantaneous decoherence event after the rephasing  $\pi$ -pulses. The MBE model fits the data very well in the low to medium gain regimes, relevant to quantum level measurements, and confirms that most of the discrepancy between the data and Ledingham's model is due to the combination of background absorption and loss.

The model does lose accuracy at high gain, where the effects of inhomogeneous driving fields, not included in the model, become significant. In reality, all  $\pi$ -pulses have a Gaussian spatial mode that is mode-matched to the collection fiber for detection. This spatial distribution means the Rabi frequency varies radially. For the inversion pulse, this results in a radially-dependent gain feature, and for the rephasing pulses, inhomogeneous rephasing. The RASE mode is defined by the effects from these pulses, and in the low gain regime, the RASE mode is well matched to the collection fiber. However, in the high gain regime, the effects of the inhomogeneous gain feature scale exponentially, leading to mode distortion and reducing the coupling efficiency to the collection fiber. Further, the refractive index of the crystal locally is dependent on gain, so a radially-dependent gain feature creates a radially dependent dispersion profile, similar to a gradiant refractive index (GRIN) lens. This changes the shape of the RASE mode, which could further affect

the fiber coupling efficiency.

Regardless of the additional effects operating in the high gain regime, we can make some initial inferences on the performance of the rephasing  $\pi$ -pulses based on Figure 6. 8% of the observed rephasing inefficiency is explained by write-time decoherence. Thus, we bound the inversion efficiency of each rephasing  $\pi$ -pulse to  $\geq 84\%$  (from the MBE model) and  $\geq 93\%$  (from the efficiency data), if the  $\pi$ -pulses were the dominant source of rephasing inefficiency.

The 81% maximum observed efficiency here includes spin-state storage and exceeds the best demonstrations observed in other solid-state systems (up to 75%, all without spin-state storage) [6, 7, 22, 39–41], and approaches those seen in atomic gases (up to 95%) [8–12]. The substantial improvement over previous RASE demonstrations (14% [32]) can be attributed to the level scheme used. All  $\pi$ -pulses were applied to transitions with weak oscillator strengths: 3.2%, 7.3%, 7.0% ( $\pi_i, \pi_1, \pi_2$ ) relative to the ASE transition (see Supplementary Information), which minimises pulse distortion when propagating through the crystal.

Further improvements to the efficiency could be achieved by two main measures. First, eliminating the remaining  $\pi$ -pulse inefficiencies by using composite pulses [42] more tolerant to pulse errors than the single, temporally square,  $\pi$ -pulses used here. Second, creating a gain profile with a more uniform radial distribution, either by composite pulses or complex hyperbolic secant pulses [23, 43, 44] for the inversion. Reducing the background absorption during the memory preparation step with better level-cleaning protocols may also improve efficiencies, but this effect is likely to be small.

In summary, the above results show that the level scheme used here is capable of high recall efficiencies in a free-space experiment, along with write and storage times that will allow the storage of many temporal modes, investigated below.

## B. Characterization of RASE

The next series of experiments characterised the performance of the RASE protocol directly. We studied correlations between the ASE and RASE windows, polarization mode mixing, and temporal mode capacity.

### 1. Correlations

The time varying correlations between ASE and RASE fields were measured to investigate whether noise was present in the signals at the classical level. The correlations were studied for a series of gains between 4 and 30 dB. For each gain level, 500 RASE shots were recorded. To calculate the correlations, first the ASE and RASE windows were digitally beaten to homodyne, with a low-pass filter applied. Then, then two windows were con-

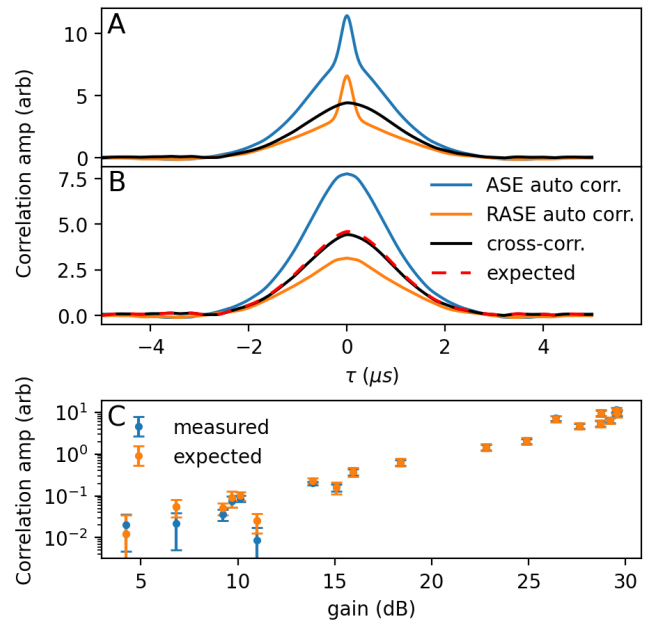


FIG. 7. **A.** shows the time-varying cross-correlation between the ASE and RASE windows and the auto-correlation for the ASE window and the RASE window. The bump in the center of the auto-correlations is the vacuum auto-correlation. **B.** shows the same graphs with the vacuum auto-correlation removed, with a time-bandwidth of 1.95  $\mu$ s. The red dashed line shows the expected cross-correlation, given the amplitude of the ASE cross-correlation and the rephasing efficiency. **C.** shows the expected and measured cross-correlation amplitudes as the gain on the ASE transition is increased.

volved,

$$C_X(\tau) = \int A(t) \cdot R(t - \tau) dt, \quad (3)$$

$$C_A(\tau) = \int A(t) \cdot \bar{A}(-(t - \tau)) dt. \quad (4)$$

Equation (3) gives the time-varying cross-correlation,  $C_X(\tau)$ , between the ASE,  $A(t)$ , and the RASE,  $R(t)$ , time windows, while Equation (4) gives the auto-correlation of the ASE window with itself. A similar expression exists for the RASE auto-correlation. The auto-correlations were used to reference the cross-correlation's amplitude back to the ASE or RASE field's amplitude. Figure 7 (A) shows the auto-correlation of both fields and the cross-correlation between them. The correlations are maximal at time  $\tau = 0$ , when the two windows are aligned. The amplitude then decays according to the bandwidth of the ensemble, with a FWHM of 1.95  $\mu$ s. The narrow peaks in the center of the auto-correlations are from a vacuum auto-correlation, broadened by the low-pass filter applied to the data. In Figure 7 B the vacuum auto-correlation has been removed by fitting a Gaussian and a Voigt profile to the vacuum and ASE/RASE auto correlations, respectively, and then subtracting the Gaussian from the data. Also shown in this figure is

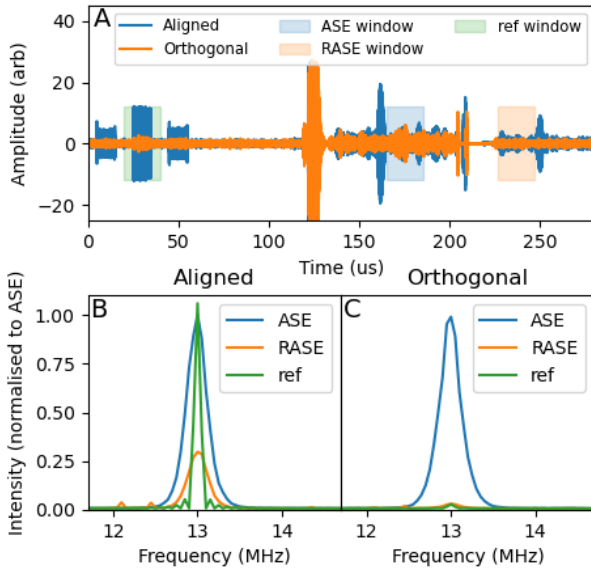


FIG. 8. **A.** High gain 4-level RASE time traces, with the local oscillator's polarization aligned with (blue) and orthogonal to (orange) the light coming out of the cryostat. The ASE and RASE windows, along with one of the reference pulses, are highlighted. **B.** and **C.**: the power spectrum of the highlighted windows for the aligned and orthogonal polarization, respectively.

the expected cross-correlation ( $C_X$ ) calculated from the vacuum-subtracted auto-correlations. Given that the RASE field's amplitude is the time-reversed complex conjugate of the ASE field scaled by the square root of the rephasing efficiency and a phase term, we can write the expected cross-correlation in terms of the ASE field,

$$C_X(\tau) = \int A(t) \cdot \sqrt{\eta} \bar{A}(-(t - \tau)) e^{i\theta} dt, \quad (5)$$

$$C_X(\tau) = \sqrt{\eta} C_A(\tau) e^{i\theta}. \quad (6)$$

Where  $\theta$  is the phase between the ASE and RASE fields. The magnitude of the cross-correlation is then the magnitude of the ASE auto-correlation scaled by the square root of the efficiency, if the two fields are perfectly correlated. Classical noise would reduce the cross-correlation. Figure 7 C. shows good agreement between the expected and measured cross-correlations, across all gains, indicating a strong correlation between the ASE and RASE fields and no measurable added classical noise.

## 2. Polarization mode mixing

Polarization mode mixing is important to characterise because, if present, it would remove polarization multiplexing as a viable method for increasing memory mode capacity, and it could introduce uncorrelated ASE/RASE

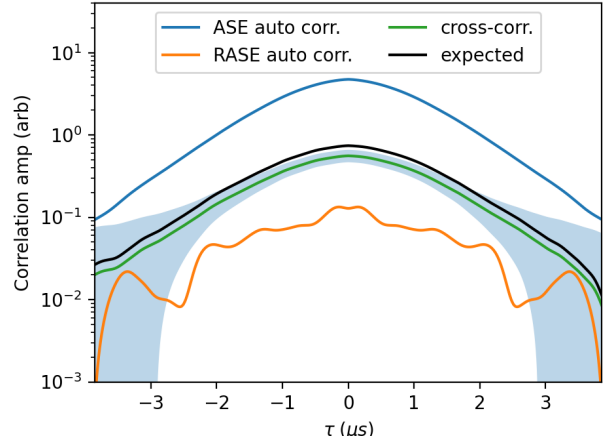


FIG. 9. Classical correlations in the weak orthogonal RASE data set, shown on a log scale. The existence of this cross correlation shows that the orthogonal RASE mode was predominately rephased from the orthogonal ASE mode, and not rephased from the aligned ASE polarization mode via some polarization mode mixing effect. The large uncertainties are due to the weak signal from this suppressed RASE mode.

fields into the detection mode. To study polarization mode mixing we recorded RASE, at maximum gain, with the heterodyne local oscillator polarization either aligned with, or orthogonal to, the polarization of the  $\pi$ -pulses. Figure 8 A. shows a time trace from both data sets, while Figures 8 B and C show the power spectrum of the ASE window, RASE window, and a reference pulse for the two polarization measurements.

The ASE field is emitted in both polarizations, consistent with our previous echo and absorption studies of this transition and propagation direction, which showed little polarization dependence [45]. In contrast, the RASE field is predominately emitted in the polarization of the  $\pi$ -pulses. This behaviour is also expected. The  $\pi$ -pulses imprint a longitudinal phase relationship on the crystal that is dependent on the crystal birefringence, with a wavelength given by the polarization beat length,  $b_L = \lambda/\Delta n$ . If the crystal length is infinite or an integer multiple of the polarization beat length, the phase matching condition dictates that RASE will only be emitted in a polarization matching the  $\pi$ -pulses. However, a small proportion of the light can be emitted in the orthogonal mode if the crystal length is not an integer multiple of  $b_L$ , as was the case here. A full refractive index tensor, along with transition electric and magnetic dipole moments, are needed to accurately model this effect, but percent-level orthogonal contributions are reasonable.

From the data in Figure 8, the orthogonal RASE mode was suppressed by  $(93 \pm 3)\%$  relative to the aligned RASE mode, while the reference pulses were suppressed by  $(99.1 \pm 0.4)\%$ . The unaccounted  $(6 \pm 3)\%$  orthogonal RASE mode can arise from either the orthogonal ASE mode (arising due to the birefringence as described

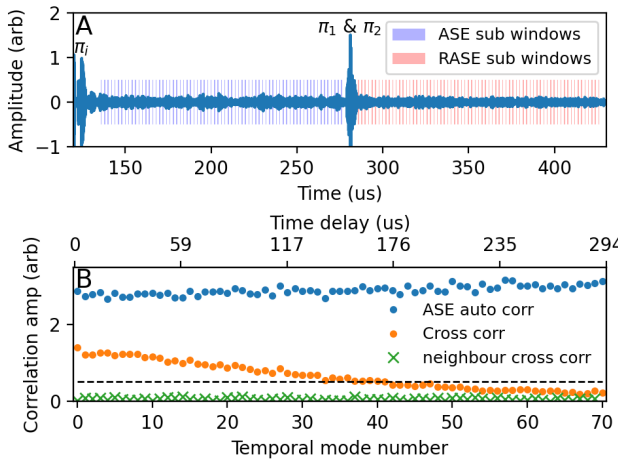


FIG. 10. Data storage capacity **A**. Demonstration of 70 RASE temporal modes, achieved by splitting the ASE and RASE windows into  $0.5\text{ }\mu\text{s}$  long sub-windows separated by  $2\text{ }\mu\text{s}$ . **B**. the RASE cross-correlation, ASE auto-correlation and the cross-correlation between an ASE window with the next RASE window, with the top x-axis showing the total delay time. The black dashed line indicates the cross-correlation amplitude  $1/e$  point, intercepting with the 40th mode.

above) or the aligned ASE mode, which would indicate the presence of polarization mode mixing. We can differentiate between these two sources by calculating the correlations between the fields. Since fast,  $\mathcal{O}(\mu\text{s})$ , polarization switching was not available, we could not directly calculate the correlation between the aligned ASE and the orthogonal RASE, but it can be inferred from the correlation of the orthogonal ASE and RASE fields, Figure 9. This correlation was strong (green line), indicating the orthogonal ASE field was the main source of the orthogonal RASE field, not mode mixing. Comparing the measured correlation to the expected correlation (black line) suggests that  $(80 \pm 10)\%$  of the  $(6 \pm 3)\%$  orthogonal RASE mode was correlated with the orthogonal ASE mode, limiting the polarization mode mixing to  $\leq 1.2 \pm 0.6\%$ . Thus, there is minimal polarization mode mixing in the experiment and the existence of the orthogonal RASE modes is not expected to affect the RASE measurements, as the heterodyne detection filters the orthogonal polarization.

### 3. Temporal multiplexing capacity

We demonstrate temporal multiplexing by subdividing the ASE and RASE temporal windows into smaller sub-windows. Figure 10 A shows a RASE data set with a  $160\text{ }\mu\text{s}$  time gap between the inversion and rephasing  $\pi$ -pulses in which 70 sub-windows, each  $0.5\text{ }\mu\text{s}$  long and separated by  $2\text{ }\mu\text{s}$ , are defined. Figure 10 B shows three correlation amplitudes for each time window: the ASE auto-correlation, the cross-correlation, and the neighbour

cross-correlation (the cross-correlation between the  $n^{\text{th}}$  ASE window and the  $(n + 1)^{\text{th}}$  RASE window). The cross-correlations decay over the  $158\text{ }\mu\text{s}$  write-time, within which 40 modes are stored, with the dashed line indicating the  $1/e$  point. This gives the memory a time-bandwidth-product of 40, in agreement with the value of 39.5 that can be calculated from the write-time and memory bandwidth (from the time-varying cross-correlation, Figure 7). Finally, the near-zero neighbour cross-correlation suggests no signs of temporal mode mixing.

Taken together, the results of this section show strong correlations between the ASE and RASE fields, with no clear evidence of mode mixing. The mode purity also allowed temporal multiplexing using the full time-bandwidth-product of the memory.

### C. Verification of quantum entanglement

The results discussed thus far have operated over a range of gains, with high gain used to achieve high efficiency, given by Equation (2), and strong signals observable at the classical level. The high gain measurements also showed no evidence of classical-level noise. However, non-classical tests are far more sensitive to classical-level noise, so the next set of measurements used a lower gain, 7 dB. In this regime, the efficiency was lower, 17%.

Non-classicality was demonstrated using the inseparability criterion for continuous variable states [46] as in previous RASE demonstrations [31, 32, 47]. The inseparability criterion uses a pair of Einstein-Podolsky-Rosen (EPR)-type operators,

$$\hat{u} = \sqrt{b}I_A + \sqrt{1-b}I_R, \quad (7)$$

$$\hat{v} = \sqrt{b}Q_A + \sqrt{1-b}Q_R. \quad (8)$$

$I$  and  $Q$  are the in-phase and out-of-phase quadrature amplitudes for both fields, with the subscripts  $A$  and  $R$  referring to ASE and RASE, respectively.  $b \in [0, 1]$  is a free parameter that weights the ASE and RASE fields. The inseparability line ( $\lambda$ ) is defined as,

$$\lambda(b) = \langle(\Delta\hat{u})^2\rangle + \langle(\Delta\hat{v})^2\rangle. \quad (9)$$

The inseparability criterion states that if  $\lambda(b) \geq 2$  for all  $b$ , then the two operators are separable, and if  $0 \leq \lambda(b) < 2$  for any  $b$ , then they are inseparable, and thus, entangled, forming a two-mode squeezed state.

Figure 11 shows the inseparability line, calculated from a 5,000-shot data set. Similar to the correlation measurements, the ASE and RASE windows were first digitally beaten to DC and low-pass filtered. A window length of  $13.2\text{ }\mu\text{s}$  and cut-off frequency of  $280\text{ kHz}$  gave the best inseparability criterion violation. The inset in Figure 11 zooms in on the inseparability criterion minimum,

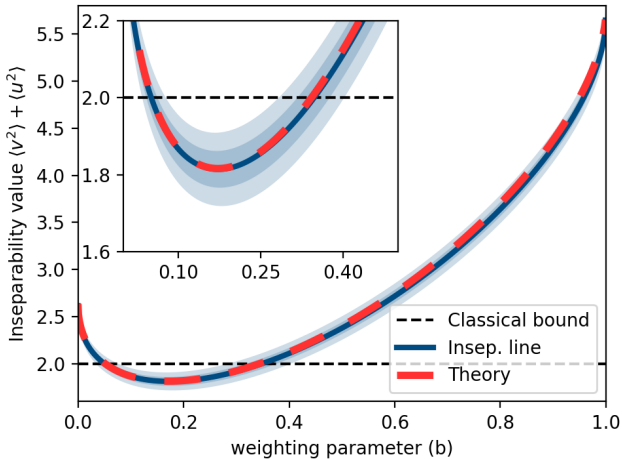


FIG. 11. Inseparability criterion violation, showing a minimum of  $1.81 \pm 0.05$  with the  $1\sigma$  and  $2\sigma$  confidence intervals shaded. The inset magnifies the inseparability minimum. The inseparability line dips below the classical boundary with a certainty of  $3.7\sigma$ . Also shown is a theoretical model of the inseparability line, red dashed line.

$1.81 \pm 0.05$  at  $b = 0.17$ . The theory line, red dash-dotted, uses a model developed by Ferguson *et al.* [31], where losses and rephasing inefficiencies are treated as beam-splitter operations that mix vacuum into the ASE and RASE fields. The model derives expressions for  $\hat{u}$  and  $\hat{v}$ ,

$$\begin{aligned} \langle (\Delta \hat{u})^2 \rangle &= b(\ell \langle I_A^2 \rangle + (1 - \ell)) \\ &+ (1 - b)\left(\ell(\eta \langle I_R^2 \rangle + (1 - \eta)) + (1 - \ell)\right) \\ &+ 2\sqrt{b(1 - b)}\ell\sqrt{\eta}\langle I_A I_R \rangle, \end{aligned} \quad (10)$$

with a similar expression for  $\langle (\Delta \hat{v})^2 \rangle$ . Here,  $\eta$  is the rephasing efficiency (17%) and  $\ell$  accounts for all losses between the crystal and the detectors (24% through cryostat windows, 50% from the heterodyne detection beamsplitter, and 20% loss due to detector quantum efficiency). The inseparability criterion is violated with a certainty of  $3.7\sigma$  and shows excellent agreement with the theoretical model, indicating the absence of mode mixing other than with the vacuum state associated with losses in the experiment.

Finally, we can infer the squeezing factor of the two-mode squeezed state was 0.4 dB at the detectors, given the inseparability minimum, 1.81. This value includes all the losses in the experiment from crystal to detector, including the heterodyne detection. We can also calculate the squeezing factor at the output of the crystal, without experimental losses, using the inseparability model to give at 1.5 dB, which is limited by the rephasing efficiency.

#### IV. DISCUSSION

In this paper we made the first demonstration of quantum state storage in erbium using an operating regime (temperature, magnetic field, choice of levels, and spectral preparation strategy) that can allow high performance across all quantum memory metrics relevant for both quantum repeater operation and LOQC. We showed non-classical correlations between time separated optical fields with a certainty of  $3.7\sigma$ ; storage efficiency up to 81%; a storage time of 25  $\mu$ s; and memory write-time of 158  $\mu$ s, giving storage of 70 distinct temporal modes with a time-bandwidth product of 40. While this performance in itself is promising for applications of  $^{167}\text{Er}$  quantum memories, more importantly, the study has allowed us to determine how to improve the critical memory parameters of fidelity, efficiency, storage time, and storage capacity, as none of these parameters are yet limited by the material properties of  $^{167}\text{Er}^{3+}:\text{Y}_2\text{SiO}_5$ . Here, we use this information to lay out the pathway for further improvement of Er-based quantum memories. We will first discuss improvements to the RASE scheme specifically, and then explain how these results are relevant to a more general-purpose, read-write quantum memory.

*Fidelity* – The inseparability condition used here to quantify the entanglement of ASE and RASE fields is not immediately translatable into fidelity, but the fact that the theoretical model, which includes no sources of infidelity, matched the data extremely well indicates the fidelity of the quantum storage step is high. The non-classical measurements support this conclusion. Infidelity arises from mixing of occupied modes into the signal, and we saw no sign of temporal mode mixing, while the polarization mode mixing was bounded above by 1.2%.

*Efficiency* – For applications, the first bar for quantum memory efficiency is 90%, because exceeding this threshold would relax the resources needed for quantum error correction [18]. In Sec. III A, we showed that the remaining inefficiency in this system is due primarily to rephasing inefficiencies, with a small contribution from background absorption. There was no optimisation of the pulse shape here for rephasing efficiency. The measures described in III A, comprise composite and complex hyperbolic secant pulses, have been successful in improving efficiency of  $\pi$ -pulses in NMR and quantum memories [23, 42–44]. Given that Ledingham’s model predicts  $> 99\%$  efficiency for perfect pulses at high gain,  $> 90\%$  efficiency is likely when these measures are applied here.

In the current setup, high efficiencies can only be reached at high gain, but placing the crystal in a Q-switchable, impedance-matched cavity [39, 40] would allow the same high efficiencies in the low-gain regime [48] needed for quantum-level measurements. Such a setup offers further improvements to take the efficiency well beyond 90%: the spatial mode distortion effects seen in the high gain regime can be avoided, and thinner crystals can be used, which then reduces the background absorp-

tion and any absorption of the rephasing  $\pi$ -pulses.

Here, for our quantum-level measurements, we chose a gain of 7 dB (and resulting efficiency of 17%) as sufficiently low to avoid classical noise. The improvements above will allow much higher efficiencies at this gain, but we also note that this was an overly conservative choice of gain, as the results of [III B](#) show minimal classical noise, even at high gain. Operating at higher single pass gain will push up both the quantum storage efficiency and squeezing factor achievable in an impedance-matched system.

*Storage time* – The 25  $\mu$ s storage time here, limited by dephasing on the hyperfine transition, is sufficient for networking demonstrations over a  $< 5$  km network, and is equivalent to the longest delay lines used in LOQC experiments. It is straightforward to extend this storage time significantly by adding rephasing pulses on the storage hyperfine transition to the RASE pulse sequence [\[49, 50\]](#). This change allows the storage time to be extended to the  $> 1$  s [\[20\]](#) hyperfine coherence time. Work to reach a storage time of 3.7 s using this approach will be reported separately.

*Mode capacity* – The temporal mode capacity shown here, determined by the write time, is ultimately limited by fundamental material properties: the uncorrelated inhomogeneous broadening on the different transitions employed. Improving the mode capacity, therefore, requires using other degrees of freedom. While it is experimentally complex to access, significant capacity is available in the spatial domain, given a spot size of 100  $\mu\text{m}^2$  compared to an average crystal size of 1  $\text{cm}^2$ . Spectral multiplexing is more straightforward. Here, it would involve simply preparing multiple spectrally resolved antiholes, and running the RASE sequence on each antihole concurrently. The preparation of multiple antiholes has already been shown in this material [\[21\]](#). For the level scheme shown here, the optical splittings between  $\pi$ -pulses and between the ASE and RASE fields limits spectral multiplexing, setting an upper bound of 95 MHz (spectra shown in Supplementary Information). Given the 95 MHz limit, and the 158  $\mu$ s write-time, the storage of  $\sim 7000$  modes is theoretically possible within a single spatial mode.

*Applications of the current system* – Since RASE combines a source and memory, it can form the basis of a quantum networking demonstration with minimal addition infrastructure. The current efficiencies and storage times are sufficient for initial demonstrations that are  $\mathcal{O}(km)$ . The underlying performance of the system is similar to, or better than, the performance seen in other recent demonstrations [\[51–55\]](#). Such a demonstration is also considerably less experimentally complicated in  $^{167}\text{Er}^{3+}:\text{Y}_2\text{SiO}_5$ , because this previous work relied on frequency conversion to interact with telecom-band pho-

tons.

*Read-write memory implementation* – The RASE protocol combines a quantum light source and quantum memory, which can be used for the state generation and initial storage steps in LOQC and quantum repeaters, but it is not a read-write quantum memory for arbitrary states. A read write memory can be used to synchronize quantum states at any point in an LOQC, for instance. This capability is provided by closely related protocols to RASE, particularly the noiseless photon echo (NLPE)[\[33, 56\]](#), which can operate using exactly the same set of levels as RASE.

RASE can be transformed into the NLPE by adding an input pulse (i.e. an I4LE), removing the inversion pulse ( $\pi_i$ ), and changing the rephasing pulse sequence from  $(\pi_1, \pi_2)$  to  $(\pi_1, \pi_2, \pi_2, \pi_1)$ , with the requirement that the wavevectors of  $\pi_1, \pi_2$  must break the phase matching conditions that produce the echo (e.g. by using counter-propagating pulses). Given the similarities between the two pulse sequences, and assuming good overlap of counter-propagating pulses, we expect NLPE to show similar performance to what is reported here in terms of storage time, write time, and lack of mode mixing. The extra pair of rephasing pulses may lower the efficiency from 81% to  $\geq 70\%$ , given the  $\geq 93\%$  bound on the rephasing  $\pi$ -pulse efficiency, assuming the memory is operated in backwards recall [\[56\]](#). The steps described above to improve the RASE performance will have a similar effect on the NLPE.

## V. CONCLUSION

We reported the first demonstration of a quantum memory protocol capable of high efficiency, fidelity and storage capacity in a telecom compatible material. We showed strong entanglement between an output state and the state retained in memory, violating the inseparability criterion by  $3.7\sigma$ . The temporal multiplexing capacity (70 modes demonstrated) was the only parameter of the memory that is reaching the fundamental material limits, but the addition of spectral multiplexing provides a data capacity up to a (calculated)  $10^4$  spectro-temporal modes per spatial mode. We achieved memory efficiencies up to 81% (in the classical regime), the highest storage efficiency seen with any rare earth quantum memory protocol. Modifications to the pulse sequences can improve this efficiency above 90% in the quantum regime, and extend the 25  $\mu$ s storage time out to the  $\mathcal{O}(1)$  s coherence times. Such a memory could exceed the performance of fiber delay lines for LOQC and allow the demonstration of global-scale quantum networks.

[1] E. Knill, R. Laflamme, and G. J. Milburn, *Nature* **409**, 46 (2001).

[2] H. Aghaei Rad, T. Ainsworth, R. N. Alexander, B. Altieri, M. F. Askarani, R. Baby, L. Banchi, B. Q. Bar-

giola, J. E. Bourassa, R. S. Chadwick, I. Charania, H. Chen, M. J. Collins, P. Contu, N. D'Arcy, *et al.*, *Nature* **638**, 912 (2025).

[3] S. Bravyi, A. W. Cross, J. M. Gambetta, D. Maslov, P. Rall, and T. J. Yoder, *Nature* **627**, 778 (2024), publisher: Nature Publishing Group.

[4] R. Acharya, I. Aleiner, R. Allen, T. I. Andersen, M. Ansman, F. Arute, K. Arya, A. Asfaw, J. Atalaya, R. Babbush, D. Bacon, J. C. Bardin, J. Basso, A. Bengtsson, S. Boixo, and Google Quantum AI, *Nature* **614**, 676 (2023), publisher: Nature Publishing Group.

[5] F. Wang, M. Ren, W. Sun, M. Guo, M. J. Sellars, R. L. Ahlefeldt, J. G. Bartholomew, J. Yao, S. Liu, and M. Zhong, *PRX Quantum* **6**, 010302 (2025).

[6] M. P. Hedges, J. J. Longdell, Y. Li, and M. J. Sellars, *Nature* **465**, 1052 (2010).

[7] D. Schraft, M. Hain, N. Lorenz, and T. Halfmann, *Phys. Rev. Lett.* **116**, 073602 (2016).

[8] M. Hosseini, B. M. Sparkes, G. Campbell, P. K. Lam, and B. C. Buchler, *Nat. Commun* **10**.1038/ncomms1175 (2011).

[9] Y.-F. Hsiao, P.-J. Tsai, H.-S. Chen, S.-X. Lin, C.-C. Hung, C.-H. Lee, Y.-H. Chen, Y.-F. Chen, I. A. Yu, and Y.-C. Chen, *Phys. Rev. Lett.* **120**, 183602 (2018).

[10] M. Cao, F. Hoffet, S. Qiu, A. S. Sheremet, and J. Laurat, *Optica* **7**, 1440 (2020).

[11] Y. Wang, J. Li, S. Zhang, K. Su, Y. Zhou, K. Liao, S. Du, H. Yan, and S.-L. Zhu, *Nat. Photonics* **13**, 346 (2019), number: 5 Publisher: Nature Publishing Group.

[12] J. Guo, Z. Wu, G. Bao, P. Yang, Y. Wu, L. Q. Chen, and W. Zhang, *Near-perfect broadband quantum memory enabled by intelligent spinwave compaction* (2025), arXiv:2505.02424 [quant-ph].

[13] K. Alexander, A. Benyamin, D. Black, D. Bonneau, S. Burgos, B. Burridge, H. Cable, G. Campbell, G. Cataiano, A. Ceballos, C.-M. Chang, S. S. Choudhury, C. J. Chung, F. Danesh, T. Dauer, and PsiQuantum team, *Nature* **641**, 876 (2025), publisher: Nature Publishing Group.

[14] N. Sangouard, C. Simon, H. de Riedmatten, and N. Gisin, *Rev. Mod. Phys.* **83**, 33 (2011).

[15] M. Razavi, M. Piani, and N. Lütkenhaus, *Physical Review A* **80**, 032301 (2009), publisher: American Physical Society.

[16] Y. Wu, J. Liu, and C. Simon, *Physical Review A* **101**, 042301 (2020), publisher: American Physical Society.

[17] W. Tittel, M. Afzelius, T. Chanelière, R. Cone, S. Kröll, S. Moiseev, and M. Sellars, *Laser Photonics Rev.* **4**, 244 (2010).

[18] S. Muralidharan, L. Li, J. Kim, N. Lütkenhaus, M. D. Lukin, and L. Jiang, *Sci Rep* **6**, 20463 (2016), number: 1 Publisher: Nature Publishing Group.

[19] T. Boettger, Y. Sun, C. W. Thiel, and R. L. Cone, in *Advanced Optical Data Storage*, Vol. 4988, edited by H. J. Coufal, A. E. Craig, and Z. U. Hasan, International Society for Optics and Photonics (SPIE, 2003) pp. 51 – 61.

[20] M. Rančić, M. P. Hedges, R. L. Ahlefeldt, and M. J. Sellars, *Nat. Phys.* **14**, 50 (2018).

[21] J. S. Stuart, M. Hedges, R. Ahlefeldt, and M. Sellars, *Phys. Rev. Research* **3**, L032054 (2021).

[22] M. M. Minnegaliev, K. I. Gerasimov, T. N. Sabirov, R. V. Urmanceev, and S. A. Moiseev, *JETP Letters* **115**, 720 (2022), publisher: Pleiades Publishing Ltd.

[23] M. M. Minnegaliev, K. I. Gerasimov, and S. A. Moiseev, *Jetp Lett.* **117**, 865 (2023).

[24] C. Li, C. Wyon, and R. Moncorge, *IEEE Journal of Quantum Electronics* **28**, 1209 (1992), publisher: IEEE ADS Bibcode: 1992IJQE...28.1209L.

[25] Y. Sun, T. Böttger, C. W. Thiel, and R. L. Cone, *Phys. Rev. B* **10.1103/PhysRevB.77.085124** (2008).

[26] M. Rancic, *High Resolution Spectroscopy of Erbium Doped Solids*, Ph.D. thesis, Laser Physics Centre, Research School of Physics and Engineering, The Australian National University (2017).

[27] E. Saglamyurek, J. Jin, V. B. Verma, M. D. Shaw, F. Marsili, S. W. Nam, D. Oblak, and W. Tittel, *Nat. Photonics* **9**, 83 (2015), 1409.0831.

[28] B. Lauritzen, J. Minář, H. de Riedmatten, M. Afzelius, N. Sangouard, C. Simon, and N. Gisin, *Physical Review Letters* **104**, 080502 (2010).

[29] P. M. Ledingham, W. R. Naylor, J. J. Longdell, S. E. Beavan, and M. J. Sellars, *Phys. Rev. A* **81**, 012301 (2010).

[30] S. E. Beavan, M. P. Hedges, and M. J. Sellars, *Phys. Rev. Lett.* **109**, 093603 (2012).

[31] K. R. Ferguson, S. E. Beavan, J. J. Longdell, and M. J. Sellars, *Phys. Rev. Lett.* **117**, 020501 (2016).

[32] C. K. Duda, K. R. Ferguson, R. L. Ahlefeldt, M. P. Hedges, and M. J. Sellars, *Phys. Rev. A* **107**, L030602 (2023).

[33] Y.-Z. Ma, M. Jin, D.-L. Chen, Z.-Q. Zhou, C.-F. Li, and G.-C. Guo, *Nat Commun* **12**, 4378 (2021), number: 1 Publisher: Nature Publishing Group.

[34] B. S. Ham and P. R. Hemmer, *Physical Review B* **68**, 073102 (2003).

[35] M. Afzelius, I. Usmani, A. Amari, B. Lauritzen, A. Walther, C. Simon, N. Sangouard, J. Minář, H. De Riedmatten, N. Gisin, and S. Kröll, *Physical Review Letters* **104**, 1 (2010), arXiv: 0908.2309.

[36] M. Gündoğan, P. M. Ledingham, K. K. Kutluer, M. Mazzera, and H. De Riedmatten, *Physical Review Letters* **114**, 10.1103/PhysRevLett.114.230501 (2015), arXiv: 1501.03980 ISBN: 9781467374750.

[37] N. Timoney, B. Lauritzen, I. Usmani, M. Afzelius, and N. Gisin, *Journal of Physics B: Atomic, Molecular and Optical Physics* **45**, 124001 (2012).

[38] K. R. Ferguson, *Generation and storage of optical entanglement in a solid state spin-wave quantum memory*, Ph.D. thesis, Laser Physics Centre, Research School of Physics and Engineering, College of Physical and Mathematical Sciences (2016).

[39] P. Jobez, I. Usmani, N. Timoney, C. Laplane, N. Gisin, and M. Afzelius, *New J. Phys.* **16**, 083005 (2014).

[40] M. Sabooni, Q. Li, S. Kröll, and L. Rippe, *Phys. Rev. Lett.* **110**, 133604 (2013).

[41] S. Duranti, S. Wengerowsky, L. Feldmann, A. Seri, B. Casabone, and H. d. Riedmatten, *Optics Express* **32**, 26884 (2024), publisher: Optica Publishing Group.

[42] M. H. Levitt, *Progress in Nuclear Magnetic Resonance Spectroscopy* **18**, 61 (1986).

[43] J. Minář, N. Sangouard, M. Afzelius, H. De Riedmatten, and N. Gisin, *PHYSICAL REVIEW A* **82**, 10.1103/PhysRevA.82.042309 (2010).

[44] F. de Seze, F. Dahes, V. Crozatier, I. Lörgeré, F. Bretenaker, and J.-L. Le Gouët, *Eur. Phys. J. D* **33**, 343 (2005).

[45] R. L. Ahlefeldt, A. Lyasota, J. Smith, J. Ren, and M. J. Sellars, *Physical Review B* **108**, 195122 (2023).

- [46] L.-M. Duan, G. Giedke, J. I. Cirac, and P. Zoller, [Phys. Rev. Lett. \*\*84\*\*, 2722 \(2000\)](#).
- [47] P. M. Ledingham, W. R. Naylor, and J. J. Longdell, [Phys. Rev. Lett. \*\*109\*\*, 093602 \(2012\)](#).
- [48] L. A. Williamson and J. J. Longdell, [New Journal of Physics \*\*16\*\*, 073046 \(2014\)](#).
- [49] Y. Ma, Y.-Z. Ma, Z.-Q. Zhou, C.-F. Li, and G.-C. Guo, [Nature Communications \*\*12\*\*, 2381 \(2021\)](#).
- [50] G. Heinze, C. Hubrich, and T. Halfmann, [Phys. Rev. Lett. \*\*111\*\*, 033601 \(2013\)](#).
- [51] M. Businger, L. Nicolas, T. S. Mejia, A. Ferrier, P. Goldner, and M. Afzelius, [Nat Commun \*\*13\*\*, 6438 \(2022\)](#), number: 1 Publisher: Nature Publishing Group.
- [52] J. V. Rakonjac, S. Grandi, S. Wengerowsky, D. Lago-Rivera, F. Appas, and H. d. Riedmatten, [Optica Quantum \*\*1\*\*, 94 \(2023\)](#), publisher: Optica Publishing Group.
- [53] C. M. Knaut, A. Suleymanzade, Y.-C. Wei, D. R. Assumpcao, P.-J. Stas, Y. Q. Huan, B. Machielse, E. N. Knall, M. Sutula, G. Baranes, N. Sinclair, C. De-Eknamkul, D. S. Levonian, M. K. Bhaskar, H. Park, M. Lončar, and M. D. Lukin, [Nature \*\*629\*\*, 573 \(2024\)](#), publisher: Nature Publishing Group.
- [54] J.-L. Liu, X.-Y. Luo, Y. Yu, C.-Y. Wang, B. Wang, Y. Hu, J. Li, M.-Y. Zheng, B. Yao, Z. Yan, D. Teng, J.-W. Jiang, X.-B. Liu, X.-P. Xie, J. Zhang, Q.-H. Mao, X. Jiang, Q. Zhang, X.-H. Bao, and J.-W. Pan, [Nature \*\*629\*\*, 579 \(2024\)](#), publisher: Nature Publishing Group.
- [55] Y. Zhou, P. Malik, F. Fertig, M. Bock, T. Bauer, T. van Leent, W. Zhang, C. Becher, and H. Weinfurter, [PRX Quantum \*\*5\*\*, 020307 \(2024\)](#), publisher: American Physical Society.
- [56] V. Damon, M. Bonarota, A. Louchet-Chauvet, T. Chanelière, and J.-L. Le Gouët, [New Journal of Physics \*\*13\*\*, 093031 \(2011\)](#).

## VI. SUPPLEMENTARY INFORMATION

### A. Field gradient model

This section details a numerical model used to describe the effects of a parabolic magnetic field gradient on the write-time and storage time of the ensemble. The field gradient exists due to inhomogeneities in the 6 T magnetic field from the superconducting solenoid. Figure 12

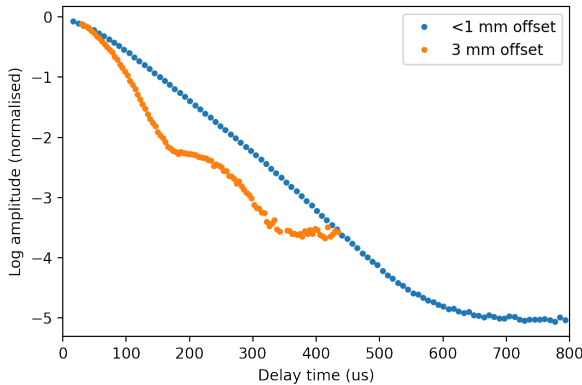


FIG. 12. Two I4LE write-time data sets, with the crystal axially displaced in the magnetic field by  $< 1$  mm (blue) and 3 mm (orange).

shows two I4LE write-time measurements. The blue data set is the write-time data presented in the main text, where the crystal was within 1 mm of the magnet center. In the orange data set, the crystal was moved 3 mm, in the axial direction, from the magnet center. In this data set, the echo decay has a very pronounced modulation, arising from the magnetic field gradient across the crystal.

The change in magnetic field shifts the hyperfine levels of the erbium ions, which causes different regions of the crystal to dephase at different rates. The dephasing leads to constructive and destructive interference between different spatial regions of the crystal.

By measuring the magnetic field, and corresponding gradient, across the crystal we determine the erbiums frequency detuning along with the density of ions at a given frequency detuning, giving an effective spectral lineshape. The echo modulation is simply the inverse Fourier transform of this lineshape. In a trivial case, a purely linear field gradient, the lineshape will be a top hat and the echo modulation follow a  $|\text{sinc}|$  function. For a parabolic field gradient, the lineshape is numerically estimated. Finally, the decays in Figure 12 are the convolution of the echo's modulation and the inhomogeneous spin dephasing [34–36].

Figure 13 shows the magnetic field as a function of axial distance from the center of the solenoid, roughly parallel with the light propagation in the main text, with the solenoids radial direction perpendicular to the laser

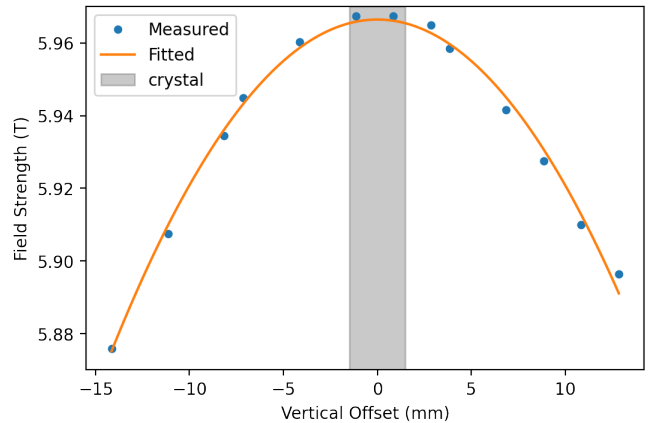


FIG. 13. Measured magnetic field as a function of axial distance, taken in the center of a 6 T magnetic field. The orange line shows a parabolic fit to the data. The grey shaded region shows the position of our 3 mm thick crystal.

beam. Given the laser beam waist,  $30 \mu\text{m}$ , is much smaller than the 3 mm length of the crystal, the radial field gradient has a much smaller effect and is ignored.

The fitted parabola in Figure 13 is then transformed into an atom detuning by,

$$B(x) = ax^2 + bx + c, \quad (11)$$

$$f(x) = g \cdot B(x), \quad (12)$$

where  $B(x)$  is the magnetic field strength,  $f(x)$  is the atoms frequency detuning, and  $g$  is the magnetic field sensitivity of the storage transition.

We now estimate the density of ions at a given detuning frequency,  $\rho(f)$ , assuming the erbium ions are homogeneously distributed through the crystal,  $\rho(x) = c$ .

$$\rho(f) \propto \rho(x) \cdot \frac{dx}{df}, \quad (13)$$

For a parabolic field gradient,  $\frac{dx}{df}$  becomes undefined at  $x = 0$ . To deal with this discontinuity the crystal was divided into finite slices in the frequency domain, with the slice boundaries chosen to avoid discontinuities.

Figure 14 shows the frequency detuning as a function of axial displacement for the write-time transitions (for both data sets in Figure 12), with the crystal location for the  $< 1$  mm data set shown in orange.

The frequency density function,  $\rho(f)$ , for the  $< 1$  mm data is shown in Figure 15. For this data set the frequency detuning is small, at most 300 Hz, compared to the 4.3 kHz inhomogeneous spin dephasing (see main text). Thus, the effect of the field gradient is small compared to the 158  $\mu\text{s}$  write-time. Figure 16 shows the two write-time decay components: inhomogeneous spin dephasing and field gradient dephasing, for the  $< 1$  mm offset (top) and 3 mm offset (bottom), respectively.

Ultimately, the effects of magnetic field gradients shown in the main text is rather minimal. However, this

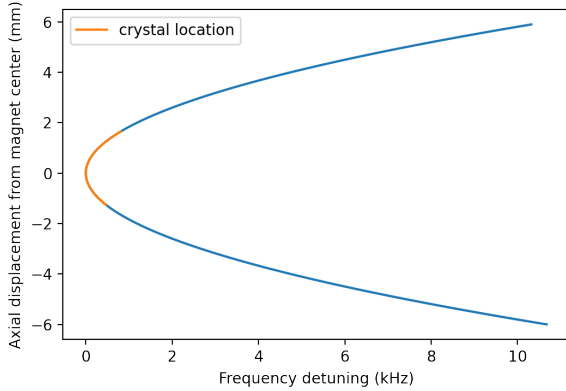


FIG. 14. Frequency detuning for the write levels as the crystal is displaced axially in the magnetic field. The orange section of the line shows the crystals position in Figure 4. Note that the parabola is slightly lopsided.

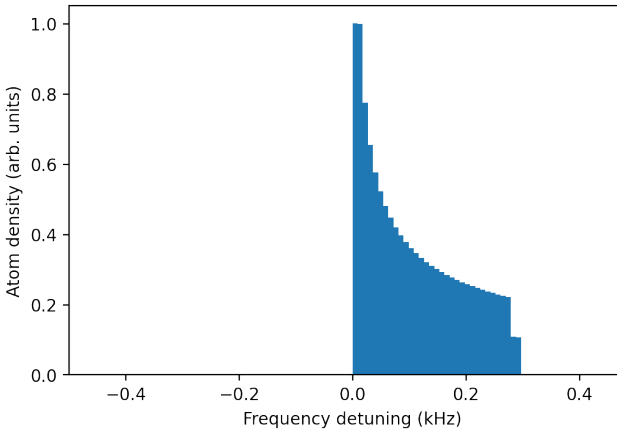


FIG. 15. Ion density at different frequency detunings, on the storage levels of the I4LE, due to a magnetic field gradient. For clarity, all the ions have the same optical transition frequency. There is a small step on the high frequency side of the graph, this is because the crystal was not perfectly centered in the field, so one edge side of the crystal had a slightly larger field gradient than the other side.

does indicate the importance of homogeneous magnetic fields, and the results shown here will be used when considering crystal size and field homogeneity. For the  $< 1$  mm data, the field gradient was  $\sim 1$  mT, and shows a small, but observable effect on the write-time.

This effect can be minimised by using thin crystals, which the main text indicates that thin crystals will be used in impedance matched cavities. Further ways to minimise this effect, if needed, are: a smaller magnetic field (Ref. [20] suggests that fields as low as 3 T could be used) or shimming gradient coils.

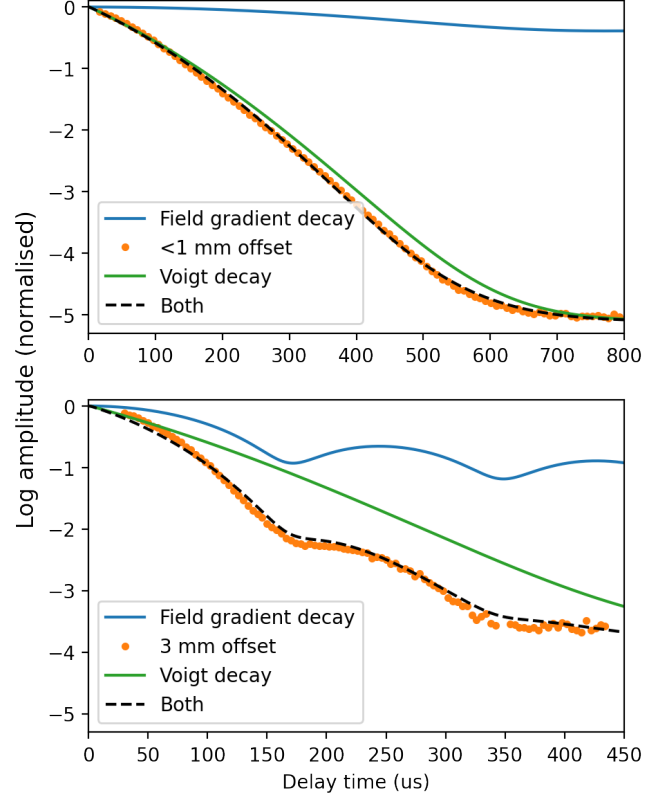


FIG. 16. Fitting for both write-time data sets. Also shown is the decay of the inhomogeneous broadening (Voigt) and the dephasing due to the field gradient.

## B. Oscillator strengths and spectra

Here, we present thermal spectra of  $^{167}\text{Er}^{3+}:\text{Y}_2\text{SiO}_5$  along with the relative oscillator strengths and relative transition frequencies of the transitions used in the RASE protocol. Figure 17 shows the spectra of  $^{167}\text{Er}^{3+}:\text{Y}_2\text{SiO}_5$

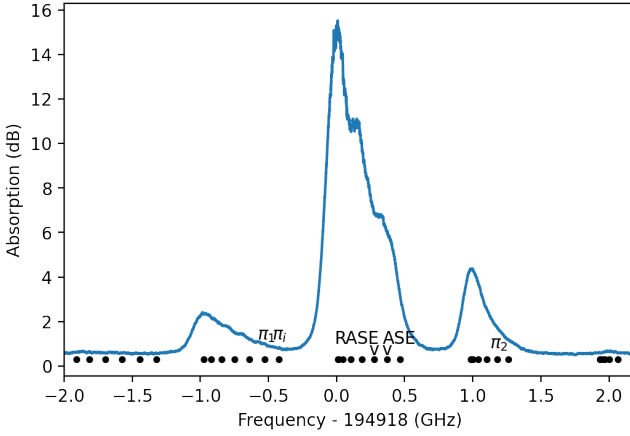


FIG. 17. 6 T site 2  $^{167}\text{Er}^{3+}:\text{Y}_2\text{SiO}_5$  spectra. Each black dot represents an optical transition, with the ASE, RASE, and  $\pi$ -pulse transitions labelled.

in thermal equilibrium, with an inhomogeneous linewidth of 150 MHz [20]. The black dots each indicate a unique optical transition and the transitions used in the RASE

transition are labelled  $\pi_i$ ,  $\pi_1$ ,  $\pi_2$ , ASE, and RASE. This figure can be used to understand the limitation of the bandwidth of the photon memory. The ultimate limit of bandwidth of a memory is the optical inhomogeneous linewidth, here 150 MHz, but there can be lower protocol- or material- dependent limits. Here, the bandwidth is limited by off-resonant excitation of other transitions during any step of the pulse sequence, as this will cause errors. For this particular level scheme, the ASE and RASE transitions are the closest, separated by 95 MHz, which defines the memory bandwidth.

$\pi$ -pulse/ transition	Relative oscillator strength (%)	Freq. (MHz) - 194918 GHz
$\pi_i$	3.2	-430.36
ASE	89.6	363.75
$\pi_1$	7.3	-538.14
$\pi_2$	7.0	974.97
RASE	81.7	268.33

TABLE I. Relative oscillator strengths and transition frequencies of the transitions used in the 4-level RASE pulse sequence. The ASE and RASE transitions are the closest to each other, split by 95.42 MHz.

Table I shows the relative oscillator strengths and transition frequencies of the transitions used in the 4-level RASE pulse sequence. As discussed in the text, the  $\pi$ -pulse transitions are all significantly weaker than the ASE and RASE transition, allowing the gain on the two output transitions to be high while the  $\pi$ -pulses experience low absorption and thus minimal distortion.